communications materials

A Nature Portfolio journal

Article

https://doi.org/10.1038/s43246-026-01110-3

# On the origin of bulk-related anisotropies in surface optical spectra



Max Großmann [1,2] ✉, Kai Daniel Hanke [2,3], Chris Yannic Bohlemann [2,3], Agnieszka Paszuk [2,3,4], Thomas Hannappel [2,3], Wolf Gero Schmidt [5] & Erich Runge [1,2]

Reflection anisotropy spectroscopy is widely used to probe the optical properties of surfaces, yet the origin of the 'bulk-related' features has been debated for decades. It is often argued that these features are related to surface-induced bulk anisotropy because they coincide with critical energies of the bulk dielectric function. Here, we show that a quantitative understanding of these features requires an explicit analysis of excitonic contributions. We introduce a layer-resolved exciton localization measure within the framework of many-body perturbation theory, enabling a direct assessment of the spatial origin of optical anisotropies. Applying this approach to arsenic-modified silicon reconstructions, we find that, depending on the surface structure, the apparent 'bulk-related' features originate predominantly from surface-localized states. Supported by low-temperature reflection anisotropy measurements, our findings challenge the traditional explanation of surface-induced bulk anisotropy and suggest that bulk-enhanced surface anisotropies also contribute to, or are responsible for, these features.

Reflection anisotropy (RA) spectroscopy (RAS) has been extensively studied and discussed for a variety of semiconductor surfaces and heterostructures over the past decades due to its importance in surface characterization and technological applications[1–20]. However, the interpretation of RAS experiments has generally been far from straightforward, as RA spectra give only indirect insights into surface structure and chemistry. Furthermore, interpreting spectra based on simplified models, such as bond polarizability is difficult and may lead to wrong results[21]. Arguably, the full potential of RAS can therefore only be realized through a strong collaboration between experimental and theoretical work, especially in understanding the complex origins of the spectral features.

Today, RAS features due to transitions between surface states are well understood and have been enormously useful in surface exploration for decades, as reviewed in detail by Weightman et al.[22]. However, a topic that has been observed for many surfaces and has been heavily debated for the past 40 years (e.g., refs. 1,23–26) is the origin of 'bulk-related' features in RA spectra, i.e., features that coincide with critical points of the imaginary part of the bulk dielectric function, often referred to as surface-induced bulk anisotropy (SIBA). Throughout this work, SIBA is used as a conventional label for such features, in line with established usage in the literature, but without implying that their microscopic origin has been established, unless explicitly stated. Irrespective of the investigated surface or specific reconstruction, e.g., Si(100)-$c(4 \times 2)$, Si(100)-$(2 \times 1)$:H and Si(100)-$(1 \times 1)$:H[12], Si(111):H and Si(110):H[13], GaAs(110) and GaAs(100)-$\beta 2(2 \times 4)$[14], GaAs(100)-$c(4 \times 4)$[15], As-rich GaAs(100)-$c(2 \times 8)$[16], ZnTe(100)[17] and InP(100)-$c(2 \times 4)$[18] the occurrence of SIBA features has been noted. Their origin is often argued to be related to "bulk-like electronic states perturbed by the surface"[18]. Specifically, it has been proposed that they may be related to strain induced by surface reconstructions, steps or dimerization via the piezo-optic effect[13] or to surface electric fields via the linear electro-optic effect[19,20]. Aspnes et al.[23] suggested that they are caused by photon-induced localization of bulk electronic states. In fact, some authors[14] have gone so far as to state: "after realizing that many RA line shapes are similar to the imaginary part of the bulk dielectric function, or to its energy derivative, it is a growing belief that surface optical spectra are mostly determined by bulk effects, and therefore, not very useful as a tool of surface characterization". While this sentiment has softened over the years, a clear explanation of SIBA features remains elusive. Throughout this work, we use the term 'bulk-related' to refer to such features, in order to remain consistent with established literature on this topic. The use of quotation marks highlights that this terminology can be misleading and does not imply a direct bulk origin. The present study focuses on how such features emerge on a microscopic level, i.e., whether they emerge directly from surface states or perturbed/extended bulk states. In this context, we define 'surface' as the reconstructed topmost atomic layer, a definition that will be used throughout the manuscript.

[1]Theoretical Physics I, Institute of Physics, Technische Universität Ilmenau, Ilmenau, Germany. [2]Center of Micro- and Nanotechnologies, Technische Universität Ilmenau, Ilmenau, Germany. [3]Fundamentals of Energy Materials, Institute of Physics, Technische Universität Ilmenau, Ilmenau, Germany. [4]BMBF Junior Research Group PARASOL, Institute of Physics, Technische Universität Ilmenau, Ilmenau, Germany. [5]Lehrstuhl für Theoretische Materialphysik, Universität Paderborn, Paderborn, Germany. ✉e-mail: max.grossmann@tu-ilmenau.de

From a theoretical point of view, it has long been recognized that excitonic effects, which are not captured by the independent particle approximation (IPA), contribute significantly to RA spectra of semiconductor surfaces[4,5,9] and may be the key to explaining 'bulk-related' features[14]. Nevertheless, only a limited number of studies[4,5,9–12] have addressed these excitonic contributions by solving the Bethe-Salpeter equation (BSE) within the framework of many-body perturbation theory (MBPT)[27]. A detailed analysis of the excitonic transitions using BSE eigenvectors[28,29] analogous to recent work on excitons near the band gap of bulk or two-dimensional materials[30–32] remains to be fully explored for surfaces. The main challenge has been the computational cost associated with the exact diagonalization of the large, nonsparse BSE-Hamiltonian matrix[5,9,33]. As a result, previous investigations have either restricted the transition space, facilitated by a favorable surface band structure[10], or employed iterative diagonalization algorithms[5,9,12], yielding RA spectra without elucidating the underlying origins of the excitonic features. Even when the BSE was exactly diagonalized[11], a characterization of the excitonic features of RA spectra was not performed.

A detailed interpretation of excitonic features, especially for the aforementioned SIBA features, through a precise methodology would be particularly important for experiments monitoring changes in RA spectra during sample growth or exposure experiments[34–37]. To address this issue, we introduce the layer-resolved exciton localization (LREL) measure as a conceptual and quantitative framework for analyzing excitonic contributions to RA spectra. LREL combines BSE eigenvectors with the state- and layer-resolved projected wave function characters, allowing us to specify from which atomic layer the excitonic contributions to the RAS originate.

While previous studies have been limited by the daunting computational demands of diagonalizing the BSE for surfaces, advances in high performance computing resources are finally making it possible to clarify the origin of the SIBA features: They allow us to accurately diagonalize the BSE and rigorously post-process the results using our LREL measure for large unit cells, i.e., the surfaces studied here. As a result, a detailed analysis of excitonic effects in semiconductor surfaces becomes possible, shedding light on the elusive origin of SIBA features. Thus, our study not only addresses a long-standing problem in the field, but also provides a recipe for the thorough analysis of surface optical spectra.

To test our method on a real system with a more challenging surface band structure than, for example, the Si(111)-(2 × 1) reconstruction[4], we focus on arsenic-modified Si(100) surfaces, which exhibit strong SIBA features. These surfaces have recently gained attention as a promising substrate for low-defect III-V-on-Si heteroepitaxy[38–42]. They have also been shown to be crucial for the development of low-cost, high-efficiency photoelectrochemical devices[43–46].

We focus on two particular Si(100) reconstructions that form during arsenic exposure under different growth conditions. The first is the Si(100)-(2 × 1):As reconstruction with two symmetric As dimers, previously studied by Kipp et al.[2], which is formed during an ultra-high vacuum (UHV) preparation using $As_4$ precursors[2,47]. The second is the Si(100)-(2 × 1):As-Si-H reconstruction, which we have recently demonstrated to occur in chemical vapor deposition (CVD) environments, where large amounts of background hydrogen and hydrogen from tertiarybutylarsine (TBA) precursors lead to the formation of a reconstruction with mixed buckled As-Si-H dimers[48]. As experimental reference, we use data measured by Kipp et al.[2] at room temperature (RT) for the Si(100)-(2 × 1):As reconstruction and performed our own low-temperature (LT) RAS measurements for the Si(100)-(2 × 1):As-Si-H reconstruction, described in the Methods section. For the sake of brevity, we will omit (2 × 1) from the notation of the surface reconstructions from now on, since all surfaces considered here share the same (2 × 1) surface unit cell.

Before introducing our analysis method and presenting results, we first outline and discuss the equations commonly used in the analysis of RA spectra. In general, RAS measures the difference between complex Fresnel reflection amplitudes $r$ along two orthogonal directions $x$ and $y$ in the surface plane of a sample

$$\frac{\Delta r}{r} = \frac{2(r_x - r_y)}{r_x + r_y} \tag{1}$$

Experimentally, the real part of the RAS is usually measured, i.e., $\mathrm{Re}(\Delta r/r)$, and often used directly for comparison with ab initio calculations for $\Delta R/R$, which refer to the reflectivity $R = |r|^2$. However, this direct comparison can lead to overestimated anisotropies because $2\,\mathrm{Re}[\Delta r/r] \approx \Delta R/R$[49]. Taking into account this factor of two, we can calculate the RAS for normally incident light using the equation established in the works of Del Sole et al.[50,51] and Manghi et al.[52]:

$$\mathrm{Re}\left[\frac{\Delta r}{r}\right] = \frac{8\pi\omega}{c}\,\mathrm{Im}\left[\frac{\Delta\alpha^{\mathrm{hs}}(\omega)}{\varepsilon^{\mathrm{b}}(\omega) - 1}\right] \tag{2}$$

Here, $\varepsilon^{\mathrm{b}}(\omega)$ is the bulk dielectric function of the substrate, and $\Delta\alpha^{\mathrm{hs}}(\omega)$ is the half-slab polarizability of the (reconstructed) surface. From an ab initio calculation of a symmetric surface slab approximating a semi-infinite crystal, $\Delta\alpha^{\mathrm{hs}}(\omega)$ is obtained from the difference of the diagonal components of the surface dielectric tensor $\varepsilon^{\mathrm{s}}_{ii}(\omega)$, i.e., $\Delta\alpha^{\mathrm{hs}}(\omega) = d\,\Delta\varepsilon^{\mathrm{s}}/2 = d\,[\varepsilon^{\mathrm{s}}_{xx}(\omega) - \varepsilon^{\mathrm{s}}_{yy}(\omega)]/2$, where $d$ is half the thickness of the surface slab[52] and mirror symmetry $z \leftrightarrow -z$ or inversion symmetry $\mathbf{r} \leftrightarrow -\mathbf{r}$ is assumed[7]. From here on, we will refer to $\Delta\varepsilon^{s}$ as the surface dielectric anisotropy.

At this point, it is beneficial to examine Eq. (2) in more detail to understand the effect of the bulk dielectric function on RA spectra. First, we decompose Eq. (2) into the real and imaginary parts of bulk and surface terms[53]

$$\mathrm{Re}\left[\frac{\Delta r}{r}\right] = \frac{4\pi\omega d}{c}\,(A \cdot \mathrm{Im}[\Delta\varepsilon^{\mathrm{s}}] - B \cdot \mathrm{Re}[\Delta\varepsilon^{\mathrm{s}}]) \tag{3}$$

where

$$A = \frac{\mathrm{Re}[\varepsilon^{\mathrm{b}}]-1}{(\mathrm{Re}[\varepsilon^{\mathrm{b}}]-1)^2+(\mathrm{Im}[\varepsilon^{\mathrm{b}}])^2}$$
$$B = \frac{\mathrm{Im}[\varepsilon^{\mathrm{b}}]}{(\mathrm{Re}[\varepsilon^{\mathrm{b}}]-1)^2+(\mathrm{Im}[\varepsilon^{\mathrm{b}}])^2}$$

Note that Eq. (3) follows directly from Eq. (2) and has previously been used in the literature to establish a relationship between the surface dielectric anisotropy and the bulk dielectric function[53–55]. Upon examining Eq. (3), it becomes apparent that the surface dielectric anisotropy $\Delta\varepsilon^{s}$ can be strongly modulated by the bulk contributions $A$ and $B$ when the real part of the bulk dielectric function is close to one while the imaginary part is small. For example, in bulk silver (see Fig. 4 in ref. 8), this phenomenon occurs around $\omega$ = 3.8 eV, where the real part of the dielectric function approaches one, and just before the onset of the $d^{10}s^1 \rightarrow d^9s^2$ absorption peak in the imaginary part. At this energy, $\mathrm{Im}[\varepsilon^{\mathrm{b}}]$ remains relatively small.

To further explore the influence of the bulk dielectric function on the RAS, we introduce a simple model system with silicon as the bulk (substrate) material. It illustrates explicitly that spectral features of a completely isotropic bulk material can show up as frequency-dependent reflection anisotropy of the surface.

In our model calculations, we systematically vary the surface dielectric anisotropy of a fictitious surface layer on top of isotropic bulk silicon. The latter is modeled via the dielectric function $\varepsilon^{\mathrm{b}}$ and $A$, $B$ measured by Aspnes and Studna[56]. We note in passing that the structures of $A$ and $B$ are similar to those of other common semiconductors such as Ge, GaAs, and GaP (see ref. 53). The surface dielectric anisotropy is modeled as a single Lorentz oscillator $\varepsilon(\omega) = \varepsilon_\infty + A[(\omega_0^2 - \omega^2) - i\gamma\omega]^{-1}$, with $\varepsilon^{\mathrm{s}}_{yy}(\omega) = 0.9\,\varepsilon^{\mathrm{s}}_{xx}(\omega)$, i.e., $\Delta\varepsilon = 0.1\,\varepsilon^{\mathrm{s}}_{xx}$, and we explore the influence of the four model parameters $(\omega_0, \varepsilon_\infty, A, \gamma)$ on the RAS. The numerical values of the model parameters and a visualization of $A$ and $B$ derived from the bulk dielectric function

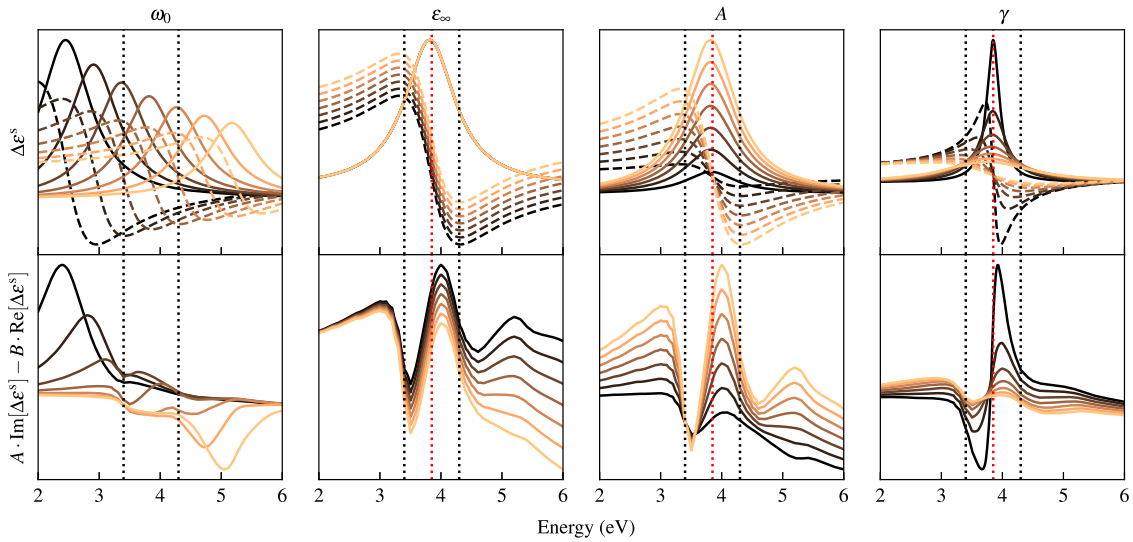


**Fig. 1 | Illustration of the effect of varying the surface dielectric anisotropy on the reflection anisotropy spectrum.** Here, silicon is used as a representative bulk material with $\varepsilon^b$ taken from Aspnes and Studna[56]. The top row shows the surface dielectric anisotropy models (see text), with each column showing variations in a specific model parameter, as indicated by the column titles. The imaginary and real parts of the surface dielectric anisotropy are represented by solid and dashed lines, respectively. The bottom row shows how the RAS, i.e., Eq. (3) without the prefactor $4\pi\omega dc^{-1}$, changes as the surface dielectric anisotropy is varied. The line colors change linearly from black to orange with increasing values of the parameter being varied. The critical-point energies of bulk silicon[79] are marked by vertical dotted black lines in all panels. In columns 2−4, a dashed red line marks the value of $\omega_0$ used for the surface dielectric anisotropy.

measured by Aspnes and Studna[56] are given in Supplementary Note 1 of the Supplementary Information. Our model can be interpreted as accounting for changes in the electronic structure at the surface of a semiconductor substrate, such as those resulting from changes in surface reconstruction due to varying growth conditions or the addition of a monolayer with anisotropic optical properties.

The model surface dielectric anisotropy and the resulting RAS, i.e., Eq. (3) without the prefactor $4\pi\omega dc^{-1}$, are shown in Fig. 1. Looking at the first column, where we vary $\omega_0$ while keeping the other parameter fixed, we see that the sign of the RAS changes depending on whether the surface dielectric anisotropy is below or above the critical points of the bulk dielectric function (indicated by the dotted black lines). When the peak of the surface dielectric anisotropy is at or between the critical points of the bulk dielectric function ($\omega_0 \in [3.4,\ 4.3]$ eV), a strong modulation of the RAS is seen, which could easily and erroneously be attributed to SIBA rather than to what could be called 'bulk-enhanced surface anisotropy' (BESA). In columns 2–4 in Fig. 1, the other model parameters are varied, while keeping $\omega_0$ fixed at 3.85 eV (dotted red lines). Generally, negative peaks are observed near the critical points of the bulk dielectric function, and the strong (positive) peak attributed to the surface dielectric anisotropy is slightly blue-shifted. Varying the other model parameters while keeping $\omega_0$ fixed shows that the position of the surface dielectric anisotropy feature has the most significant influence on the RAS, while other parameters primarily affect its amplitude. In summary, the model results demonstrate that the surface dielectric anisotropy may be strongly modulated by the bulk dielectric function, depending on the relative position of the spectral features of the bulk and the surface. This interaction complicates the interpretation of RA spectra, especially when investigating SIBA features. Therefore, a more comprehensive analysis of RA spectra incorporating the surface dielectric anisotropy, derived from ab initio calculations is called for.

In an ab initio context and taking into account excitonic effects (electron-hole interactions), the surface dielectric anisotropy is calculated using the surface dielectric tensor, which is obtained here by solving the BSE in the Tamm-Dancoff approximation (TDA)[29,57], see Methods for details. The diagonal components of the surface dielectric tensor are then calculated as follows:

$$\varepsilon^s_{ii}(\omega) = 1 + \frac{8\pi e^2\hbar^2}{m_0^2}\sum_{\Lambda} O^{\Lambda}_{ii} \sum_{\beta=\pm 1} \frac{1}{E^{\Lambda} - \hbar\beta(\omega + i\gamma)} \tag{4}$$

where $E^{\Lambda}$ are the exciton excitation energies (BSE eigenvalues) and $O^{\Lambda}_{ii}$ are the oscillator strengths along Cartesian direction $i$. Here $\gamma$ is a phenomenological broadening parameter that accounts for the finite lifetime and damping of excitonic states, and is, in practice, just a small real number (see Methods). The oscillator strength $O^{\Lambda}_{ii}$ is defined as:

$$O^{\Lambda}_{ii} = \frac{1}{\Omega}\left|\sum_{vc\mathbf{k}} F^i_{vc\mathbf{k}} A^{\Lambda}_{vc\mathbf{k}}\right|^2 \tag{5}$$

where $A^{\Lambda}_{vc\mathbf{k}}$ are the normalized excitonic wave function coefficients (BSE eigenvectors) obtained from the diagonalization of the BSE Hamiltonian[29] with $\sum_{vc\mathbf{k}}|A^{\Lambda}_{vc\mathbf{k}}|^2 = 1$, and $\Omega$ is the unit cell volume. The sum in Eq. (5) extends over all vertical valence-to-conduction transitions ($v \to c$) at each k-point $\mathbf{k}$ considered in the calculation. The quantity $F^i_{vc\mathbf{k}} = (f_{c\mathbf{k}} - f_{v\mathbf{k}})M^i_{vc\mathbf{k}}/(\epsilon_{v\mathbf{k}} - \epsilon_{\mu\mathbf{k}})$ includes the transition matrix elements $M^i_{vc\mathbf{k}} = \langle c\mathbf{k}|\hat{v}_i|v\mathbf{k}\rangle$ of the velocity operator $\hat{v}$ along the Cartesian direction $i$, the Fermi occupation function $f_{n\mathbf{k}}$, and Kohn-Sham states $|n\mathbf{k}\rangle$ with eigenvalues $\epsilon_{n\mathbf{k}}$ ($n = v, c$) obtained from density functional theory (DFT) or $GW$ calculations.

In Eq. (5), we can see that, for each exciton $\Lambda$, all considered transition matrix elements $M^i_{vc\mathbf{k}}$ contribute with a weight corresponding to the associated normalized BSE eigenvectors $A^{\Lambda}_{vc\mathbf{k}}$. This complicates the assignment of spectral features to specific states considerably.

For this reason, so-called "fatband analyses" of excitonic transitions are often employed in studies of bulk and two-dimensional materials (see, e.g., Fig. 2 in ref. 31 and Fig. 3 in ref. 32). In the fatband representation of a band structure, the "fatness" (e.g., band thickness or marker size) of the valence and conduction bands is proportional to $|A^{\Lambda}_{vc\mathbf{k}}|^2$. In practice, one first selects a particular exciton state of interest, i.e., $\widetilde{\Lambda}$, and calculates $|A^{\widetilde{\Lambda}}_{vc\mathbf{k}}|^2$ for all

transitions (indexed by $v$, $c$, and $\mathbf{k}$) included in the BSE Hamiltonian. Then, for each transition, the corresponding valence and conduction bands in the band structure are "highlighted" proportional to $|\widetilde{A^{\Lambda}_{v\mathbf{k}}}|^2$. The highlighted Kohn-Sham (KS) states can then be assigned to individual atoms or specific orbitals by projecting them onto local orbitals, providing valuable insight into the structure of individual excitons. However, analyzing RA spectra in this way becomes impractical because, as will be seen later, many excitons often contribute to a specific spectral feature, rendering such an approach cumbersome and inefficient.

For this reason, we introduce the layer-resolved exciton localization (LREL) measure

$$\mathrm{LREL}_{\Lambda,\alpha} = \sum_{v\mathbf{k}} |A^{\Lambda}_{v\mathbf{k}}|^2 P^{\alpha}_{v\mathbf{k}} P^{\alpha}_{c\mathbf{k}} \tag{6}$$

where $P^{\alpha}_{n\mathbf{k}}$ is the layer-resolved projected wave function character of KS state $|n\mathbf{k}\rangle$ ($n = v, c$). Here, the index $\alpha$ refers to a particular layer in the surface slab, and should not be confused with the half-slab polarizability $\alpha^{\mathrm{hs}}(\omega)$. The definition of the LREL is motivated by the general form of the excitonic wave function[57]. It quantifies the contribution of each slab layer, $\alpha$, to a given exciton, $\Lambda$, by weighting the layer projections of the valence (hole) and conduction (electron) states, $P^{\alpha}_{v\mathbf{k}}$ and $P^{\alpha}_{c\mathbf{k}}$, with the corresponding excitonic coefficients $|A^{\Lambda}_{v\mathbf{k}}|^2$ for all transitions included in the BSE Hamiltonian.

In addition, inspired by the fatband analysis introduced above, we define complementary LREL measures to provide separate insight into the spatial distributions of holes and electrons, corresponding to valence band (VB) and conduction band (CB) contributions, respectively

$$\mathrm{LREL}^{\mathrm{VB}}_{\Lambda,\alpha} = \sum_{v\mathbf{k}} |A^{\Lambda}_{v\mathbf{k}}|^2 P^{\alpha}_{v\mathbf{k}} \tag{7}$$

where $\mathrm{LREL}^{\mathrm{CB}}_{\Lambda,\alpha}$ is defined analogously with $P^{\alpha}_{v\mathbf{k}}$ replaced by $P^{\alpha}_{c\mathbf{k}}$.

Similar to the fatband analysis briefly described above, the LREL measure (and its complementary versions) now allows us to quantify how much each layer $\alpha$ of a surface slab contributes to the exciton $\Lambda$ at energy $E^{\Lambda}$. Since it involves only reciprocal space quantities, it is easy to compute even for many excitons without having to use, for example, high-dimensional excitonic wave functions on a real-space grid.

In this study, $P^{\alpha}_{n\mathbf{k}}$ is obtained as follows: (i) We calculate the orbital- and site-projected partial wave function character for KS state $|n\mathbf{k}\rangle$, i.e., $C^{\beta}_{lm,n\mathbf{k}} = |\langle Y^{\beta}_{lm}|n\mathbf{k}\rangle|^2$ with spherical harmonics $Y^{\beta}_{lm}$ centered on site $\beta$, as implemented in the Vienna Ab initio Simulation Package (VASP)[58,59]. (ii) For each site $\beta$, the sum over all orbitals $\sum_{lm} C^{\beta}_{lm,n\mathbf{k}}$ is calculated. (iii) By summing the contributions of the individual atoms $\beta$ within the layer $\alpha$ of the surface slab, we obtain $P^{\alpha}_{n\mathbf{k}}$. The calculation settings used to obtain $C^{\beta}_{lm,n\mathbf{k}}$ are given in the Methods Section. The bottom and top layers (hereafter referred to as S for surface) correspond to the surface reconstruction and consist of either As-As or As-Si-H dimers, depending on the reconstruction, while the remaining layers consist of two silicon atoms each.

It is important to note that the numerical values of the projections implicitly depend on several parameters, most notably the projection radii around the atomic sites. Here, the radii provided by the projector augmented wave pseudopotentials (PAW)[60] for each atomic species were used, thereby ensuring consistency with the basis functions and maintaining accuracy without the need for manual adjustments. For any reasonable choice of projection radii, the LREL should be sufficiently accurate to enable a quantitative analysis of the contributions of the different layers and thus insight into the spatial localization of excitonic effects without the need for more complex projection methods. Each set of projections $P^{\alpha}_{n\mathbf{k}}$ is normalized such that $\sum_{\alpha} P^{\alpha}_{n\mathbf{k}} = 1$ for every state $|n\mathbf{k}\rangle$, to further minimize residual dependence on the specific choice of projection radii. Before continuing, we note two almost trivial observations in passing: (i) Any other method of projecting a KS state onto localized orbitals, i.e., obtaining $P^{\alpha}_{n\mathbf{k}}$, can be used to calculate the LREL. (ii) The LREL can also be used to analyze RAS features in an atom- or orbital-resolved fashion by omitting the sum over all atoms in a layer or over orbitals, respectively.

To make it easier to interpret the LREL for a fixed exciton $\Lambda$, we introduce the normalized LREL

$$\mathrm{NLREL}_{\Lambda,\alpha} = \frac{\mathrm{LREL}_{\Lambda,\alpha}}{\sum_{\alpha} \mathrm{LREL}_{\Lambda,\alpha}} \tag{8}$$

and analogously for the VB and CB version of the LREL. The $\mathrm{NLREL}_{\Lambda,\alpha}$ is now directly proportional to the percentage of how much layer $\alpha$ contributes to the exciton $\Lambda$. Throughout the following, the term NLREL refers to the normalized general quantity $\mathrm{NLREL}_{\Lambda,\alpha}$ defined in Eq. (8). Explicit references to the VB and CB components are denoted as $\mathrm{NLREL}^{\mathrm{VB}}_{\Lambda,\alpha}$ and $\mathrm{NLREL}^{\mathrm{CB}}_{\Lambda,\alpha}$, respectively.

Before discussing the results, we briefly comment on how to interpret the different LREL measures. The general LREL formulation in Eq. (6) is physically well behaved and provides a straightforward interpretation of where an exciton is localized within the slab. When the valence and conduction states of an exciton are localized within the same layer, $\mathrm{LREL}^{\mathrm{VB}}_{\Lambda,\alpha}$, $\mathrm{LREL}^{\mathrm{CB}}_{\Lambda,\alpha}$, and $\mathrm{LREL}_{\Lambda,\alpha}$ exhibit coincident maxima, allowing for a clear interpretation. For excitons extending over several layers, the separated $\mathrm{LREL}^{\mathrm{VB}}_{\Lambda,\alpha}$ and $\mathrm{LREL}^{\mathrm{CB}}_{\Lambda,\alpha}$ distributions correctly reveal the spatial separation of the hole and electron. However, in this situation, analyzing only one of these distributions, e.g., $\mathrm{LREL}^{\mathrm{VB}}_{\Lambda,\alpha}$, could misleadingly suggest a localized exciton, whereas examining the general LREL clarifies that the excitation is delocalized across layers. Therefore, the separate $\mathrm{LREL}^{\mathrm{VB}}_{\Lambda,\alpha}$ and $\mathrm{LREL}^{\mathrm{CB}}_{\Lambda,\alpha}$ measures should be regarded as complementary tools that individually resolve the spatial contributions of the hole and electron. Degenerate or nearly degenerate excitons may exhibit slightly different LREL patterns because their eigenvectors can differ even at identical excitation energies. In such cases, averaging $\mathrm{NLREL}_{\Lambda,\alpha}$ over the corresponding degenerate subspace—or a small energy window—provides a robust representation. In practice, however, the LREL maps in this study include several thousand excitons. Therefore, regardless of how they are treated, the presence of a few degenerate states does not affect the overall trends or the conclusions drawn.

## Results

### Electronic structure and optical properties

Before discussing the electronic and optical properties of the Si(100):As and Si(100):As-Si-H surface reconstructions, we briefly summarize the theoretical framework and approximations used in this study. All ground state properties were computed using the hybrid functional HSE06[61,62], which provides a reliable approximation to the quasiparticle band structure of the large surface slabs considered here, as fully converged $GW$ calculations would be computationally prohibitive. The quantitative accuracy of this approximation was recently validated by Sagredo et al.[63], who demonstrated that HSE06 reproduces the fundamental bulk and surface band gaps of the reconstructed Si(111)-(2 × 1) and Ge(111)-(2 × 1) surfaces within ~0.1 eV of $GW$ and experimental results. A similar observation was made for the $wz$-GaN($1\bar{1}00$) surface by Landmann et al.[10]. All excitonic calculations were performed by solving a so-called model BSE based on HSE06 single-particle energies and wave functions. In this framework, the electron-hole interaction is described using an analytical model for the static dielectric screening, which was shown to reproduce the excitonic features of the monohydride Si(100) surface within ~0.1 eV of fully screened BSE calculations[33]. Together, these approximations yield a physically meaningful, yet computationally tractable, description of the ground state and excitonic structure of large surface models. Further methodological details and convergence tests are provided in the Methods section and Supplementary Note 2, respectively.

Figure 2 provides an overview of the atomic arrangements, surface band structures, and RA spectra. The side and top views of the Si(100):As and Si(100):As-Si-H surface reconstructions, highlighting their similar, yet distinct, atomic configurations, are shown in Fig. 2a, b, e, f, respectively.

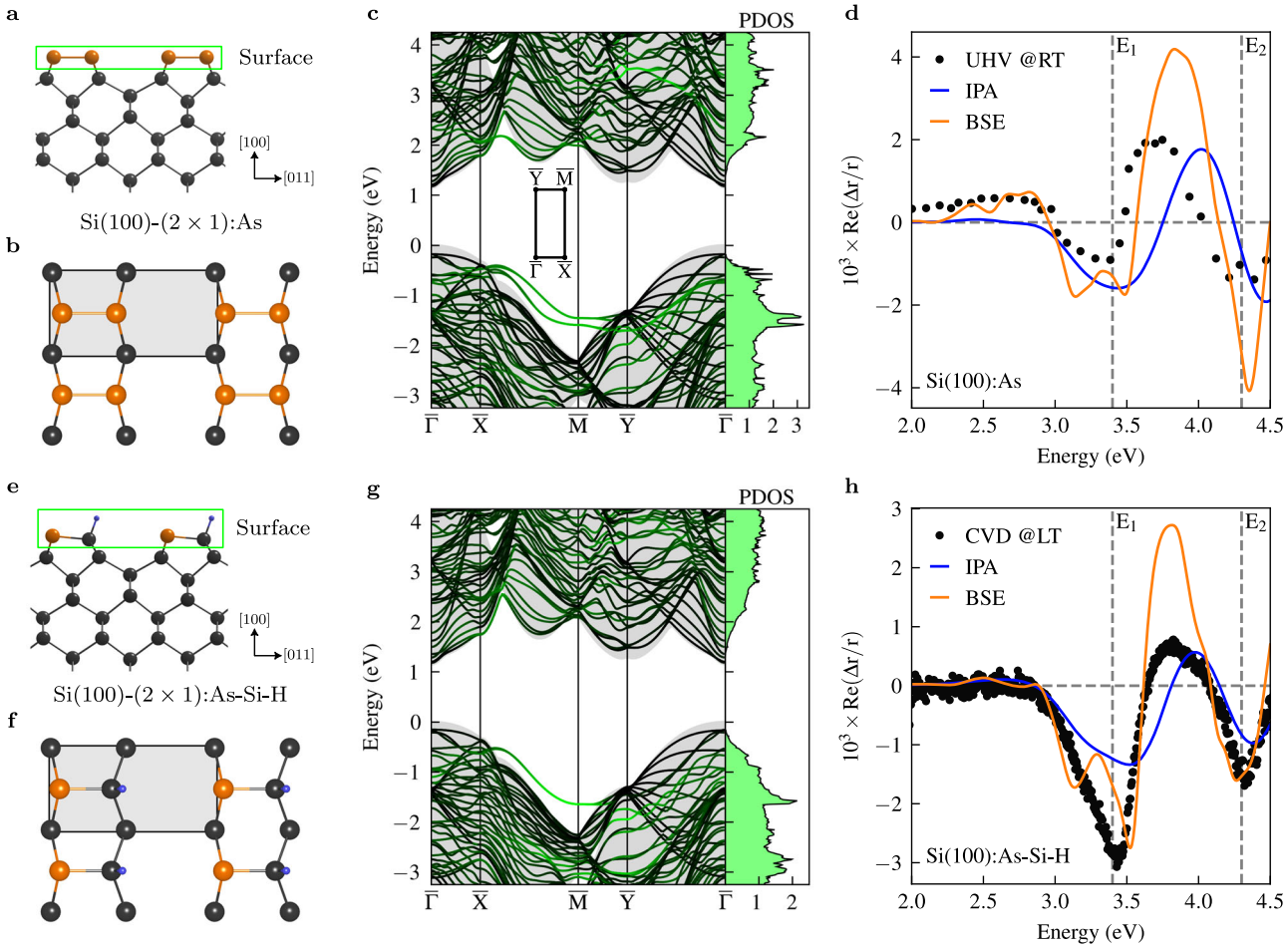


**Fig. 2 | Structural, electronic, and optical properties of the Si(100):As and Si(100):As-Si-H surface reconstructions.** The top row, i.e., **a**–**d**, shows the results for Si(100):As, and the bottom row, i.e., **e**–**h**, for Si(100):As-Si-H. **a**, **e** Side view of the atomic arrangement of the surface reconstructions. **b**, **f** Top view along the [100] axis of the surface reconstructions. The (2 × 1) surface unit cell is highlighted in gray. **c**, **g** Surface band structures calculated using the hybrid functional HSE06 and 20-layer slabs, with partial density of states (PDOS, in states/eV) projected onto the surface atoms highlighted in **a**, **e**, respectively. The color of the bands corresponds to $P^{\alpha}_{n\mathbf{k}}$ for the highlighted surface layer in **a**, **e** where green indicates a high surface contribution and black indicates no surface contribution. The projected band structure of bulk silicon is shaded in light gray in the background. The (2 × 1) surface Brillouin zone is shown in **c**. **d** Comparison of reflection anisotropy (RA) spectra obtained from experimental measurements and theoretical calculations for the Si(100):As surface reconstruction. The experimental data were adapted from Kipp et al.[2] and were measured at room temperature. The theoretical RA spectrum with the blue line represents a calculation within the independent particle approximation (IPA), while the orange line is obtained by solving the Bethe-Salpeter equation (BSE), see text and the Methods section. The critical points of the imaginary part of the bulk dielectric function of silicon are marked by vertical dashed gray lines[79], highlighting SIBA features. **h** Same as **d**, but for the Si(100):As-Si-H surface reconstruction. The experimental RA spectrum was measured by us at low temperatures (LT), see text and the Methods section.

Surface band structures calculated with the hybrid functional HSE06 (see Methods) are shown in Fig. 2c, g, where the bands are colored by $P^{\alpha}_{n\mathbf{k}}$ to highlight the contributions from the surface (green). Both reconstructions exhibit surface states close to the valence bands between the $\overline{\mathrm{X}}$ and $\overline{\mathrm{M}}$ points in the (2 × 1) surface Brillouin zone. Comparing both, it can be observed that the surface states are directly related to the arsenic atom in the surface structure, as the Si(100):As with two As atoms shows two distinct surface bands, while the Si(100):As-Si-H with only one As atom shows one surface band. This observation is further supported by the Si(100):As-Si-H surface band structure shown in Supplementary Note 3, where the bands are colored by $\sum_{lm} C^{\mathrm{As}}_{lm,n\mathbf{k}}$.

In Fig. 2d, h, we present the experimental and calculated RA spectra. The measured spectra of both reconstructions exhibit pronounced features at $E_1$ and $E_2$ that are also observed in measurements of other Si(100) reconstructions[12]. The microscopic origin of these features, often explained in terms of SIBA, will be investigated later. Comparing the measured RAS of the Si(100):As at RT with our LT RAS measurements of the Si(100):As-Si-H, we observe a slight blue shift and an increase in the feature amplitudes. This observation is more apparent when comparing the Si(100):As-Si-H measured at process temperatures with the LT measurements shown in Supplementary Note 8. The observed spectral changes in our LT measurements can be explained as follows: While in bulk silicon thermal expansion causes only a small redshift of the indirect band gap of about 2.5 meV when the temperature is increased from 0 to 400 K, electron-phonon interactions induce a substantial decrease of the indirect band gap of 0.05–0.1 eV[64], explaining the shift in peak positions. The reduction of exciton-phonon scattering at lower temperatures, confirmed by ab initio calculations for silicon and h-BN[65], leads to the observed reduced peak broadening, i.e., the increase of feature amplitudes. In addition, the larger feature amplitudes in the LT measurement are also likely enhanced by a higher surface order, increasing the optical anisotropy.

Having presented the experimental data, we now turn to the spectra obtained from theory. The spectra shown are calculated using Eq. (2), where $\varepsilon^{\mathrm{b}}$ and $\Delta\alpha^{\mathrm{hs}}$ are obtained from consistent theory levels starting from HSE06 calculations, i.e., by calculating the IPA dielectric function or solving the BSE. As shown several times before[4,5,9,12], we again observe that excitonic effects included in the BSE (orange) strongly modulate (red shift and line shape change) the RA spectra compared to IPA calculations (blue). The

calculated BSE spectra closely match the experimental data. However, it could be argued that the BSE prediction for the Si(100):As surface reconstruction agrees with the measurement by Kipp et al.[2] not much better than the IPA spectra. Closer inspection of Fig. 2d reveals that the apparent agreement between the IPA and the experiment is mostly confined to the region around the direct gap of silicon At photon energies above 3.5 eV, the BSE more accurately reproduces the experimental peak positions, while the IPA peaks are strongly blue-shifted. Although the overall spectral agreement may appear similar, solving the BSE remains essential for a consistent microscopic interpretation since it mixes and redistributes optical transition weights according to Eqs. (4)–(5), a coupling absent in the IPA. Comparing the two surface reconstructions, we notice a reversal in the amplitude ratio of the peaks at $E_1$ and $E_2$, a trend also suggested by experimental data. However, a LT measurement of Si(100):As would be required to fully validate this theoretical observation.

At this point, we need to comment on the double peak visible at $E_1$ in both BSE calculations (orange lines in Fig. 2d, h). A similar feature has been observed and extensively discussed by Albrecht et al.[66] for the calculated dielectric function of bulk silicon, where it was referred to as a 'k-point ripple', i.e., a numerical artifact resulting from an insufficiently dense k-point grid.

To verify whether the double peak originates from incomplete k-point grid convergence, we performed additional calculations for the Si(100):As and Si(100):As-Si-H surface reconstructions, see Supplementary Note 2. For these, we used PBEsol wave functions with scissored energies and a reduced transition space in the BSE Hamiltonian. Additionally, we omitted transitions with independent-particle energy differences greater than 5 eV, whereas the production calculations shown here used a threshold of 10 eV, as described in the Methods section. These compromises were necessary in order to make calculations with denser k-point grids computationally feasible. The results confirm that the double peak around $E_1$ gradually merges into a single, smooth feature as the k-point grid density increases. However, even when doubling the k-point grid, full convergence was not achieved. Thus, achieving full convergence would require prohibitively dense k-point grids. For the current surface slabs, each containing 36 silicon atoms, these would already render the necessary HSE06 ground state calculation challenging.

We note that simply omitting the HSE06 starting point is also not an option. Although the scissor-corrected PBEsol spectra reproduce the qualitative trends, they do not match the experimental data as well as the spectra obtained from an HSE06 ground state, as shown in Supplementary Note 2. This largely stems from the fact that the scissor operator, which is commonly used in RAS literature[8,12,67,68] to approximate *GW* corrections, is an oversimplified description of quasiparticle shifts (cf. refs. 63,69).

Ideally, an exact diagonalization of the BSE Hamiltonian that includes the full transition space on an extremely dense k-point grid would provide spectra, as well as excitonic wave function coefficients, $A^{\Lambda}_{vc\mathbf{k}}$, for the LREL analysis presented below. However, such calculations are currently computationally prohibitive for the investigated surfaces. Therefore, we adopted a setup with a sufficiently large transition space to cover the energy range of interest, as well as k-point grids dense enough to ensure qualitative convergence, while remaining computationally feasible. The residual 'k-point ripples' caused by limited Brillouin-zone sampling only affect the fine structure and peak amplitudes, but not the qualitative spectral shape or its physical interpretation. A detailed discussion and illustrations of these convergence tests are provided in Supplementary Note 2.

## Exciton analysis

As demonstrated by our toy model in the introduction, analysis of RA spectra alone provides limited insight into the origin of RAS features, especially SIBA features, as BESA effects may shroud their origin (cf. Fig. 1). To address this, we focus directly on the surface dielectric anisotropy $\Delta\varepsilon^{s}$. To simplify the analysis, we consider only excitons that contribute strongly to the RAS, defined as those with $|O^{\Lambda}_{xx} - O^{\Lambda}_{yy}| > \mathcal{T}$, where $\mathcal{T}$ is a threshold set to the average contribution of all excitons within the RAS energy range (see Supplementary Note 4 for details). Even with this constraint, approximately $10^4$ excitons remain for the analysis for each surface reconstruction. In the upper panels of Fig. 3a, d, we show the surface dielectric anisotropy for both reconstructions, demonstrating that our exciton subset already accurately reproduces the surface dielectric anisotropy. Furthermore, the lower panels of Fig. 3a, d show that individual excitons do not dominate the contributions to each RAS feature. Instead, each feature results from a complex summation of positive and negative contributions, only emerging when all excitons are considered together. Note that the imaginary part of the surface dielectric anisotropies already looks remarkably similar to the RA spectra shown in Fig. 2d, h, with negative anisotropies at $E_1$ and $E_2$. Therefore, we conclude that the SIBA features seen in the RAS in Fig. 2d, h are not only caused by the BESA effect visible in the model system (cf. Fig. 1). To investigate the microscopic origin of these features in the imaginary part of the surface dielectric function, we now focus on a detailed analysis of the contributing excitons.

First, we illustrate how a conventional fatband analysis and our NLREL measure can be used to analyze the origin of individual excitons. To do this, we selected one exciton $\widetilde{\Lambda}$ for each surface reconstruction, highlighted in orange in the bottom panels of Fig. 3a, d. Figure 3b, e show the corresponding surface band structures, with the projection $P^{\alpha}_{n\mathbf{k}}$ onto the surface layer highlighted in green (cf. Fig. 2d, g). We have added circles to the surface band structures for all transitions contributing to the oscillator strength, whose size is proportional to $|A^{\Lambda}_{vc\mathbf{k}}|^2$, while their color indicates the projection: black circles correspond to bulk states, and green circles represent states localized on surface atoms. The NLREL measure (black), as well as its complementary VB (orange) and CB (blue) versions, for the selected excitons are shown in Fig. 3c, f.

For the Si(100):As reconstruction (Fig. 3, top row), we have chosen an exciton with strong contributions from surface states. The fatband representation of the surface band structure shown in Fig. 3b, highlights the localization of this particular exciton at surface states throughout the whole surface Brillouin zone (green circles), with some contributions from bulk states between the $\overline{Y}$ and $\overline{\Gamma}$ points (black circles). This observation is directly supported by the NLREL plot in Fig. 3c, where the main contribution to NLREL originates from the topmost layer, confirming a surface-localized exciton. A closer look at the VB and CB contributions reveals that both the hole and the electron are localized directly at the surface.

For the Si(100):As-Si-H reconstruction shown in the bottom row of Fig. 3, we have chosen an exciton with strong bulk contributions. The fatband representation of the surface band structure in Fig. 3e shows much more pronounced bulk transitions between the $\overline{Y}$ and $\overline{\Gamma}$ points, visible as black circles. Again, the NLREL in Fig. 3f reflects this, showing that the exciton is more localized in the center of the slab compared to the surface layer, with layer contributions increasing as one goes deeper into the slab. The complementary VB and CB NLREL measures follow the same trend. Here one should not be surprised that the NLREL, as well as its VB and CB versions, in Fig. 3f is not symmetric around the center of the slab. Although the slabs are constructed symmetrically, with identical reconstructions on both sides, a slight offset arises when aligning the surface dimers in the [011]–[001] plane. This produces a residual asymmetry along the $[0\bar{1}1]$ direction and, when the alignment is reversed, vice versa, as illustrated in Supplementary Note 5. This small geometric mismatch results in slight differences between the top and bottom surfaces of the slabs. These differences are not usually noticeable in total energy or band structure calculations, but are revealed by the LREL analysis, highlighting the sensitivity of the method.

In summary, one could use the presented fatband analysis in conjunction with our NLREL measures to study the localization of individual excitons. However, this is impractical for the subset of $10^4$ excitons that all contribute to the RAS in some non-trivial way (see the lower panels of Fig. 3a, d). Therefore, we use the NLREL maps shown in Fig. 4, which considerably streamline the analysis. For each surface reconstruction, Fig. 4 displays NLREL maps based on the general definition as well as the complementary VB and CB versions, enabling a direct comparison between the

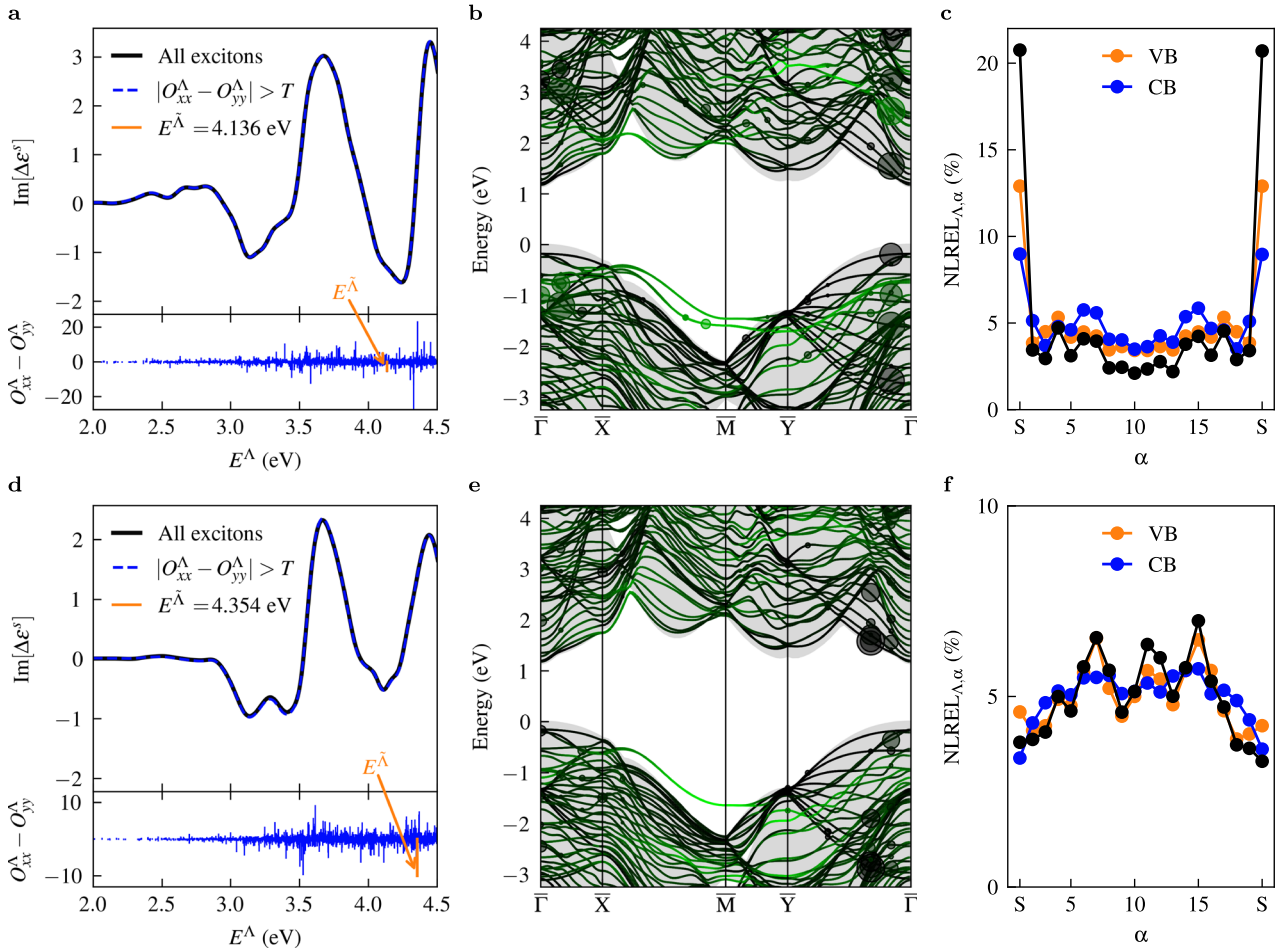


**Fig. 3 | Illustration of individual excitons contributing to the surface dielectric anisotropy of the Si(100):As and Si(100):As-Si-H surface reconstructions.** The top row (**a**–**c**) corresponds to the Si(100):As surface reconstruction, while the bottom row (**d**–**f**) shows results for the Si(100):As-Si-H surface reconstruction. **a**, **d** Upper panel: Surface dielectric anisotropy $\Delta\varepsilon^s$ calculated using all excitons (solid black line) and only those with a significant contribution to $\Delta\varepsilon^s$ (dashed blue line), see text. Lower panel: Anisotropy of oscillator strengths for excitons that significantly contribute to $\Delta\varepsilon^s$. A particular exciton $\tilde{\Lambda}$ is highlighted in orange (see arrow) and further analyzed in the following columns. **b**, **e** Fatband analysis of the exciton $\tilde{\Lambda}$ highlighted in orange in the lower panels of **a**, **d**, respectively. The underlying surface band structures have already been shown and explained in Fig. 2c, g. The size and color of the circles correspond to $|A^{\Lambda}_{vc\mathbf{k}}|^2$ and $P^{\alpha}_{n\mathbf{k}}$, respectively. A large radius indicates a large contribution of a particular KS state to exciton $\tilde{\Lambda}$. Green indicates a high surface contribution, while black indicates no surface contribution. **c**, **f** Normalized layer-resolved exciton localization (NLREL, black), together with the complementary valence band (VB, orange) and conduction band (CB, blue) versions, for the excitons $\tilde{\Lambda}$ highlighted in orange in the lower parts of **a**, **d** shown as a function of layer index $\alpha$ of the symmetric slab. "S" indicates the surface layers.

correlated exciton localization and the separate spatial distributions of the hole and the electron.

However, before discussing the actual NLREL maps, it is worth contemplating what one would expect these maps to look like, especially around the SIBA features at $E_1$ and $E_2$. Recalling the quote about the origin of the SIBA features, i.e., "bulk-like electronic states perturbed by the surface" from ref. 18 and the conclusion drawn from ref. 5: "It is shown that excitonic effects via strong modifications of the optical response of surface-modified bulk wave functions determine largely the line shape of the optical features", we would expect the following: Features in the surface dielectric anisotropy shown in Fig. 3a, d at $E_1$ and $E_2$ would be localized in layers deeper in the slab toward the 'bulk' region (slab center), caused by perturbations of the bulk wave function by the surface reconstructions. Other features may originate directly from the surface and, in these cases, the NLREL map would show strong localization at or just below the surface.

Looking at the NLREL maps in Fig. 4, our expectations are not met. In the Si(100):As surface reconstruction, almost all of the excitons above 2 eV are localized at the surface. The few excitons below 2 eV are localized in the 'bulk' region of the slab, while having almost no optical anisotropy, as can be seen by looking at the surface dielectric anisotropy in the upper panel of the left column of Fig. 4. The complementary VB and CB NLREL maps show a similar trend. For the Si(100):As-Si-H surface reconstruction, the NLREL maps for excitons below 2.5 eV are somewhat similar to those of the Si(100):As reconstruction. Again, these excitons have a vanishing contribution to the surface dielectric anisotropy. When comparing the NLREL maps for both surfaces above 2.5 eV, differences become apparent, especially when comparing the CB states of the excitons. In the Si(100):As-Si-H surface reconstruction, the CB contributions appear nearly uniform across all layers, and no strong surface or bulk localization is visible. However, the VB states are more localized at the surface, while all other layers have a small and similar contribution, similar to the Si(100):As surface reconstruction. Overall, the NLREL maps of the Si(100):As-Si-H surface reconstruction exhibit a more delocalized character with no strongly pronounced surface or bulk localizations. After comparing the NLREL maps of both surfaces, it is clear that the excitons of the symmetric dimer motif of the Si(100):As surface reconstruction are much more localized at the surface than those of the asymmetric Si(100):As-Si-H surface reconstruction, yet their surface dielectric anisotropies are remarkably similar. In both systems, we also find that the surface contribution tends to weaken slightly as one goes to higher energies, i.e., approaching the $E_2$ peak.

Now that we have discussed the NLREL maps and highlighted their differences, we question the term 'SIBA' commonly used to label features

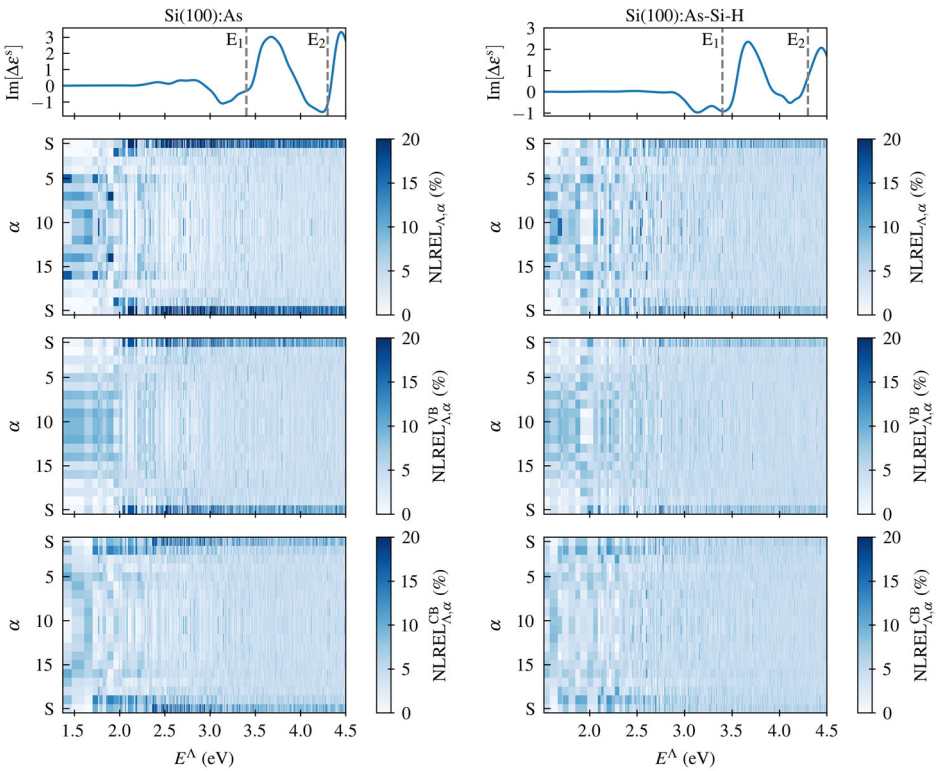


**Fig. 4 | Surface dielectric anisotropy and normalized layer-resolved exciton localization for the Si(100):As and Si(100):As-Si-H surface reconstructions.** The upper panel row illustrates the surface dielectric anisotropy, and the lower panels show the NLREL maps calculated using Eqs.((6) −(8). Left column: Si(100):As surface reconstruction. Right column: Si(100):As-Si-H surface reconstruction. In the upper panels, the critical points of the imaginary part of the bulk dielectric function of silicon are marked by vertical dashed gray lines[79]. The maximum of the NLREL color bars is limited to 20% to facilitate comparison between the two reconstructions, as only a few excitons in the Si(100):As surface reconstruction have layer localizations above this threshold.

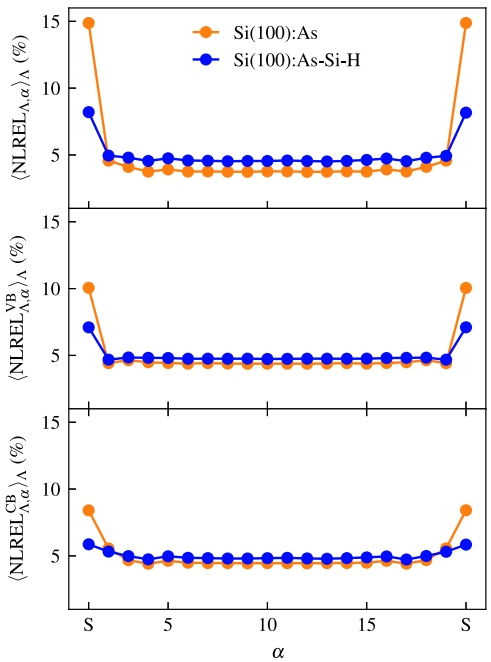


**Fig. 5 | Energy-averaged normalized layer-resolved exciton localization.** Energy averages of the NLREL maps shown in Fig. 4 for the Si(100):As (orange) and Si(100):As-Si-H (blue) surface reconstructions.

that coincide with the critical energies of the bulk dielectric function, since strong bulk contributions are missing from both 'SIBA' features in the NLREL maps, at least for the Si(100):As surface reconstruction. One could argue, however, that in the case of the Si(100):As-Si-H reconstruction, the features in the surface dielectric anisotropy around $E_1$ and $E_2$ may still be labeled 'SIBA' because many bulk-like states from many layers in the slab contribute to the surface dielectric anisotropy. No clear surface localization is visible, yet no clear localization of excitons in the 'bulk' region of the slab is visible either. The previously proposed picture of "bulk-like electronic states perturbed by the surface"[18] may still be correct, but in the broader sense that many states, independent of the layer, are perturbed by the surface. Looking at the Si(100):As surface reconstruction, the general labeling of features that coincide with the critical energies of the bulk dielectric function as 'SIBA' breaks down completely because most of the excitons contributing to the surface dielectric anisotropy are localized at the surface. Both of the above observations become even clearer when looking at the energy-averaged NLRELs in Fig. 5. Here, the difference between the surface contributions and all other layers is much smaller for the Si(100):As-Si-H surface reconstruction than for the Si(100):As surface reconstruction.

As a side note, it would be interesting to know how these NLREL maps would look if the layer size were increased drastically. At present, we are computationally limited in this regard. However, we have checked the NLREL maps for slabs with only 10 layers using the same calculation parameters and observed very similar results, as illustrated in Supplementary Note 2.

### Deciphering optical anisotropy of Si(100):V surfaces

Having shown that the NLREL maps can be used to identify the spatial origin of features in the surface dielectric anisotropies, and that the origin of 'SIBA' features is strongly system dependent, the physical effects behind them remain elusive. In particular, the cause of the strong surface localization of excitons above 2 eV in the Si(100):As deserves further investigation. To gain insight into the mechanism behind this localization, we performed further calculations on Si(100)-(2 × 1):V surface reconstructions with symmetric dimers. Specifically, we repeated all presented calculations for six additional systems. For three of them, we kept the Si(100):As geometry and replaced the As atoms with other group V atoms, i.e., P, Sb, and Bi. We will refer to these systems as Si(100):V@As (V = P, Sb, Bi) and again omit the (2 × 1) from the surface reconstruction notation. The pseudopotentials for all group V atoms have the same valence electron configuration and differ only in the treatment of their core electrons and atomic size. The

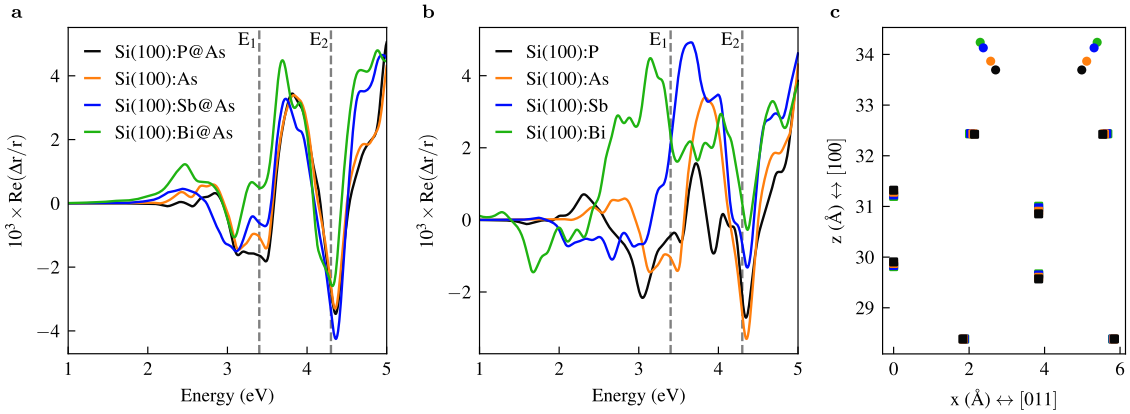


**Fig. 6 | Reflection anisotropy spectra and atomic structure of Si(100):V surfaces.** **a** RA spectra for Si(100):V@As surfaces calculated with fixed Si(100):As geometry. **b** RA spectra for the relaxed Si(100):V surfaces. **c** Structural view (of the *xz* plane spanned by the [011] and [100] vectors) of the top layers of the relaxed Si(100):V systems. Square markers denote silicon atoms, while circular markers denote group V atoms, as indicated by the color coding, which is consistent across all panels.

other three systems also follow the motif of a Si(100):As surface reconstruction with a symmetric group V dimer in a $(2 \times 1)$ supercell, but in this case their geometries were relaxed and they are referred to as Si(100):V. The calculations for the six additional surfaces were performed with the same parameters as the previous ones for consistency, see Methods.

First, we comment on the Si(100):V@As surfaces calculated with a fixed Si(100):As geometry. Looking at their RA spectra in Fig. 6a, we observe that they all look remarkably similar, and, interestingly, the $E_1$ anisotropies follow the order of the electronegativities of the group V elements, suggesting at least a small contribution of electric-field-induced anisotropy to the RAS[19,20]. The associated surface band structures, surface-projected density of states, and NLREL maps shown in Supplementary Note 6 are also quite similar. In particular, the surface band structures show a strong similarity, with only moderate differences in the gap between the two surface states propagating within the bulk band gap close to the valence bands between the $\overline{\mathrm{X}}$ and $\overline{\mathrm{M}}$ points. This may be explained by the following simple argument: The geometry of the Sb and Bi dimers is strongly compressed (cf. Fig. 6c), relative to their relaxed geometries, leading to an increase in the 'band gap' of their associated surface states, similar to the expected increase in band gap when a solid is compressed. As a result, their surface states resemble those of the As dimer. For the P dimer, the opposite geometric mismatch applies.

Looking at the RA spectra in Fig. 6b for the relaxed Si(100):V geometries shown in Fig. 6c, we observe a strong change in the spectra below the $E_2$ feature. Now that the dimers are relaxed (decrease in P-P bond distance, increase in Sb-Sb and Bi-Bi bond distances, cf. Fig. 6c), the relative energetic position of the associated surface states changes, leading to shifts in either the valence- or conduction-band-derived surface states. Indeed, as shown in Supplementary Note 6, the surface bands shift toward the bulk band gap throughout the surface Brillouin zone. This changes the transition space and thus the excitonic structure, which can be observed as features at lower energies in the RA spectra around and below $E_1$. This enhanced contribution of surface states to the RA spectra and surface dielectric anisotropy is further highlighted by the corresponding NLREL maps in Supplementary Note 6.

Comparing the RAS (and additional illustrations in Supplementary Note 6) of the constrained and relaxed Si(100):V surfaces reveals the following: (i) Surface geometry is clearly the most dominant influence on RA spectra as it affects all parts of the electronic and derived optical properties. This even concerns the localization of the excitons that contribute most to the optical anisotropies. (ii) The $E_1$ feature in the RA spectrum of Si(100):As is coincidentally at the $E_1$ energy of bulk silicon and is therefore unrelated to 'SIBA', i.e., "bulk-like electronic states perturbed by the surface"[18], as it originates from surface states. This is further emphasized by the fact that the shape and position of this feature changes drastically in all other relaxed Si(100):V surfaces. (iii) The $E_2$ feature is clearly visible as a pronounced peak in all RA spectra (and surface dielectric anisotropies, see Supplementary Note 6). We therefore argue that this feature is a mixture of some surface contributions causing intensity changes and contributions from deeper layers, since surface contributions tend to weaken at higher energies around $E_2$ in all NLREL maps (see Fig. 4 and Supplementary Note 6). In addition, the BESA effect highlighted in the simple model system, cf. Fig. 1 and associated text, likely also contributes to the presence of the $E_2$ feature in all systems.

## Discussion

Our results provide insight into the long-standing debate on the origin of 'bulk-related' anisotropies in surface optical spectra. Traditionally, such features have been attributed to SIBA, i.e., "bulk-like electronic states perturbed by the surface"[18].

First, we use a simple model system to show that these apparent 'SIBA' features may arise from what we call bulk-enhanced surface anisotropy (BESA). Obviously, a closer examination of the surface dielectric anisotropy is needed to gain thorough insight into the microscopic origin of these features. Building on this, we perform an ab initio analysis of the excitonic contributions to the surface dielectric anisotropy of the technologically relevant arsenic-terminated Si(100) surface reconstruction utilizing the framework of MBPT. We introduce the LREL measure, which allows us to obtain a layer-resolved map of exciton origins, thereby disentangling the contributions of surface and subsurface states to the RA spectra. Again, our findings challenge the simple SIBA picture, as excitonic contributions to 'bulk-related' features in RA spectra can be of different origins. For example, in the Si(100):As surface reconstruction, most excitons contributing to the optical anisotropy are localized directly at the surface, whereas they are rather delocalized in the Si(100):As-Si-H surface reconstruction. In the latter case, one could indeed speak of a SIBA effect.

The comparison of NLREL results for constrained and relaxed Si(100):V surface reconstructions shows that the surface localization of anisotropy-related excitons, in fact, depends sensitively on the structural details of the surface. These comparisons further underscore the complex relationship between electronic structure and measured optical anisotropy. Even spectral features that appear similar can originate from excitons with markedly different spatial characteristics depending on the specific surface reconstruction. This emphasizes that optical anisotropy is a highly material- and system-dependent property. The example of the Si(100):As and Si(100):As-Si-H surface reconstructions presented here clearly illustrates this point, as even minor atomic rearrangements can qualitatively change the microscopic mechanism underlying a given RAS feature. Recognizing the complexity of optical anisotropy, it becomes apparent that searching for a simple, universal explanation is unrealistic and contrary to the rich diversity of surface physics.

Having established this inherent complexity, we proceed to a more general classification of the possible microscopic origins of RAS features. In this study, we identify three possible origins of RAS features that were previously attributed to SIBA: (i) BESA effects, where the bulk dielectric function strongly modulates the optical anisotropy, as illustrated in Fig. 1; (ii) features from surface states that coincidentally appear at bulk energies, as clearly seen in the Si(100):As surface reconstruction; and (iii) SIBA effects in the true sense of the word, as observed, e.g., in the Si(100):As-Si-H surface reconstruction. The present findings thus underline that a general classification of optical anisotropies at bulk critical-points energies as SIBA does not take into account the complex origin of surface optical spectra. Rather, a detailed exciton-resolved analysis is indispensable for a proper understanding of RA spectra.

The generality and simplicity of our LREL method make it readily applicable to other semiconductor surfaces and heterostructures. By directly quantifying the contributions from individual atomic layers, our approach allows one to disentangle the relative roles of surface and subsurface states in optical spectra and provides a quantitative framework to re-examine features in the optical anisotropy of previously studied systems.

While the LREL analysis framework is generally independent of the underlying electronic structure method, the accuracy of its results ultimately depends on the level of theory used to compute the excitonic eigenvectors. Future work should therefore aim to evaluate the performance of hybrid functional and model screening approaches for additional material classes beyond monohydride Si(100)[33], Si(111) and Ge(111)[63], *wz*-GaN($1\bar{1}00$)[10], and the surfaces investigated in this study. An especially promising direction would be to investigate the optical anisotropies of technologically relevant III-V semiconductors on silicon substrates[42,70]. Additionally, as computational capabilities advance, the framework should be expanded toward a full *GW*+BSE treatment of the electronic and excitonic structure, along with methods that enable the analysis of larger and more complex surface reconstructions. These advancements will enhance the accuracy and applicability of the LREL approach in describing and understanding the microscopic origin of surface optical anisotropies.

In summary, the present work shows that 'bulk-related' anisotropies in surface optical spectra do not necessarily originate from the bulk. In fact, they may arise directly from surface reconstruction or be attributed to what we refer to as 'bulk-enhanced surface anisotropies', challenging the conventional interpretation linking these features to bulk-like electronic states perturbed by the surface. Therefore, we argue that the term 'bulk-related' should not be used generically to describe such features in reflection anisotropy spectra, unless their microscopic origin has been confirmed through many-body calculations, equivalent first-principles analyses, or possible future experiments. This is because the term may invoke erroneous connotations. Instead, spectral structures should be identified by their energetic position or other neutral labels.

By introducing a versatile, general methodology for analyzing exciton localization, our work paves the way for a refined interpretation of surface optical responses that fully accounts for the complex interplay between surface chemistry, excitonic effects, and bulk contributions. We anticipate that these findings will spur further experimental and theoretical efforts to unravel the intricacies of surface optical phenomena.

## Methods

### Ab initio calculations

DFT and MBPT calculations were performed with a modified version of VASP 5.4.4[58,59], which uses a plane-wave basis and the projector augmented-wave method[60]. Details about the code modifications, which only affect the output routines of the BSE calculations, can be found in Supplementary Note 4. To clearly outline the calculation steps and their corresponding parameters, we first describe the ground state calculations that form the basis of the MBPT calculations.

First, the total energy of bulk silicon was converged with respect to the plane-wave cutoff and k-point grid using PBEsol[71,72] as the exchange-correlation functional, chosen for its accuracy in describing bulk and surface geometries. A cutoff energy of 400 eV and a 12 × 12 × 12 Γ-centered k-point grid were sufficient to converge the total energy of bulk silicon within 1 meV, see Supplementary Note 2. After full structural relaxations for several lattice constants, i.e., relaxing the unit cell shape and atomic positions for each lattice constant, the equilibrium lattice constant was obtained by fitting a parabola to the total energy versus lattice constant curve, yielding 5.436 Å. For the geometry optimizations, a convergence threshold for all forces of $10^{-3}$ eV/Å was used. Using the obtained PBEsol lattice constant, we modeled the surfaces as 20-layer, symmetric, non-vicinal slabs containing 36 silicon atoms separated by 16 Å of vacuum. As with the previous bulk calculation, we converged the total energy with respect to the plane-wave cutoff and k-point grid, finding that a cutoff of 400 eV and a 6 × 12 × 1 Γ-centered k-point grid ensured convergence within 1 meV. The vacuum size was converged with respect to the total energy, finding that a vacuum size of more than 10 Å was sufficient to achieve convergence of the total energy within 1 meV. Nevertheless, we adopted a vacuum size of 16 Å for all surfaces. The slab thickness, expressed as the number of silicon layers, was converged with respect to the surface energy using the method of Fiorentini and Methfessel[73], indicating that at least 10 silicon layers were sufficient for convergence within 1 meV. To ensure complete convergence, all slabs in this study consisted of 18 silicon layers (see Supplementary Note 2 for convergence tests). In line with the calculations for bulk silicon, all surface slabs were relaxed until the forces on all atoms were below $10^{-3}$ eV/Å.

For excited state calculations, accurately describing the unoccupied states is essential to obtaining reliable optical spectra. Since RA spectra require evaluating both the bulk dielectric function, $\varepsilon^{\mathrm{b}}(\omega)$, and the surface dielectric tensor $\varepsilon^{\mathrm{s}}_{ii}(\omega)$ at the same theoretical level (see Eqs. (2–3)), they must be computed within the same computational framework. Because the surface cells are large, certain approximations are required to keep the calculations tractable. To approximate quasiparticle wave functions and energies, which are normally obtained from computationally demanding and difficult-to-converge *GW* calculations, we employed the hybrid functional HSE06[61,62]. This functional provides an accurate and efficient approximation to *GW* calculations, as demonstrated by Sagredo et al.[63]. HSE06 calculations were performed for both bulk silicon and all surface slabs using the PBEsol-optimized geometries and convergence parameters established above.

For the IPA spectra presented in Fig. 2, we computed $\varepsilon^{\mathrm{b}}(\omega)$ and $\varepsilon^{\mathrm{s}}_{ii}(\omega)$ in the IPA[74] at the HSE06 level using a 6 × 12 × 1 Γ-centered k-point grid and a Lorentzian broadening of $\gamma = 0.1$ eV. For the spectra including excitonic effects and the LREL analyses, we solved the BSE[27] within the TDA[57], starting from HSE06 eigenvalues and wave functions. Note that the TDA is known to produce only minor quantitative differences compared to the full BSE for a variety of bulk semiconductors and insulators, including silicon[75,76]. The static dielectric screening was represented by the analytical model introduced by Bechstedt et al.[77], a well-established approximation in the RAS community[33]. The parameters of this model depend on the static dielectric constant, $\varepsilon_\infty$, and the static $\mathbf{G} = \mathbf{G}'$ part of microscopic dielectric function, $\varepsilon^{-1}_{\mathbf{G},\mathbf{G}}(\omega = 0)$, of bulk silicon. Both were calculated at the HSE06 level using the same calculation parameters as before. Further details regarding the model dielectric screening are given in Supplementary Note 7.

For bulk silicon, the BSE Hamiltonian included 4 occupied and 12 unoccupied KS orbitals on a dense 24 × 24 × 24 Γ-centered k-point grid. For the surfaces, 36 occupied and 36 unoccupied orbitals were included on a 6 × 12 × 1 Γ-centered grid. Transitions with independent-particle energy differences greater than 10 eV were excluded from the BSE Hamiltonian (`OMEGAMAX`=10). With the calculation parameters described above, we solved the BSE for bulk silicon and the investigated surfaces to obtain $\varepsilon^{\mathrm{b}}(\omega)$ and $\varepsilon^{\mathrm{s}}_{ii}(\omega)$, respectively, applying a Lorentzian broadening of $\gamma = 0.1$ eV, consistent with the IPA calculations. The convergence of the BSE results with respect to the k-point grid, as well as the influence of slab thickness on spectra and the NLREL, is analyzed in detail in Supplementary Note 2.

The orbital- and site-projected partial wave function characters, i.e., $C^{\beta}_{lm,n\mathbf{k}}$, required for the LREL analysis, were calculated using the VASP input tags `LORBIT=11` and `RWIGS=-1`.

### Sample preparation and measurements

We used *p*-doped Si(100) substrates with a 6° offcut angle towards the [011] direction to prepare an A-type[41] Si(100)-(1 × 2):As-Si-H surface, analogous to ref. 48. Here, we want to emphasize that the difference between (1 × 2) and (2 × 1) affects the orientation of the dimers along or perpendicular to the step edges of a vicinal surface. Therefore, this should be regarded as only an "experimental" detail. This difference is well illustrated in Fig. 1 of ref. 41. However, throughout the rest of this study, we always refer to a (2 × 1) reconstruction, since all ab initio calculations have been performed for non-vicinal surfaces, making this distinction irrelevant. The samples were prepared using an $H_2$-based horizontal AIX-200 metalorganic CVD (MOCVD) reactor (Aixtron SE). The entire MOCVD process was monitored in situ by RAS (LayTec EpiRAS-200). The Si(100) substrates here were first deoxidized by annealing under constant hydrogen flow for 30 min at 1000 °C and 950 mbar in an MOCVD. Subsequently, the surface was prepared by exposure to tertiarybutylarsine (TBAs) at 800 °C and 950 mbar. Here, a sequence of opening and closing the TBAs source was applied while maintaining a constant hydrogen flow[41]. This stepwise exposure increases the surface order, and exposure to TBAs prepares double layer steps on the surface, resulting in more pronounced RAS peak amplitudes. After exposure, the samples were cooled under constant hydrogen flow and RA spectra were recorded at 597 K as shown in Supplementary Note 8.

After preparation, the samples were first transferred to a cryostat (Montana Instruments Cryostation) using an MOCVD-to-UHV shuttle to prevent surface contamination[78]. Here, a custom copper cryostat head was first cooled by a closed-loop helium setup that reduced the pressure inside the cryostat from HV to UHV as it cooled. The sample, mounted on a molybdenum carrier, was then inserted into the copper cooling head while a series of LT RA spectra were acquired at a sample temperature of approximately 50 K. Details regarding sample temperature estimation are given in Supplementary Note 8. Following the LT RAS measurements, additional low-energy electron diffraction (LEED) and X-ray photoelectron spectroscopy (XPS) measurements were performed to ensure that the sample was not contaminated during transfer or while in the cryostat (see Supplementary Note 9). For this purpose, the sample was transferred from the LT RAS setup to a LEED system (SPECS ErLEED 100) and an XPS system (monochromated Al-K$\alpha$, SPECS Focus 500/Phoibos 150/1D-DLD-43-100).

## Data availability

The data that support the findings of this study are available from the corresponding author upon reasonable request.

## Code availability

Density-functional theory and many-body perturbation theory calculations were performed using the licensed software VASP (version 5.4.4), available from https://www.vasp.at, with minor modifications to the output routines for BSE calculations, as described in Supplementary Note 4. Custom post-processing scripts were used to analyze the resulting output files and to compute the quantities discussed in this work. These scripts rely on the structure of standard and modified VASP outputs and are therefore not publicly available. The code is available from the corresponding author upon reasonable request and is subject to the licensing terms of the underlying software.

Received: 3 April 2025; Accepted: 9 February 2026;
Published online: 26 February 2026

## References

1. Aspnes, D. E. & Studna, A. A. Anisotropies in the above—Band-gap optical spectra of cubic semiconductors. *Phys. Rev. Lett.* **54**, 1956–1959 (1985).
2. Kipp, L., Biegelsen, D. K., Northrup, J. E., Swartz, L.-E. & Bringans, R. D. Reflectance difference spectroscopy: Experiment and theory for the model system Si(001):As and application to Si(001). *Phys. Rev. Lett.* **76**, 2810–2813 (1996).
3. Uwai, K. & Kobayashi, N. Surface termination effect on reflectance spectra of GaAs. *Phys. Rev. Lett.* **78**, 959–962 (1997).
4. Rohlfing, M. & Louie, S. G. Excitons and optical spectrum of the Si(111) − (2 × 1) Surface. *Phys. Rev. Lett.* **83**, 856–859 (1999).
5. Hahn, P. H., Schmidt, W. G. & Bechstedt, F. Bulk excitonic effects in surface optical spectra. *Phys. Rev. Lett.* **88**, 016402 (2001).
6. Chandola, S. et al. Structure of Si(111)-In nanowires determined from the midinfrared optical response. *Phys. Rev. Lett.* **102**, 226805 (2009).
7. Hogan, C., Del Sole, R. & Onida, G. Optical properties of real surfaces from microscopic calculations of the dielectric function of finite atomic slabs. *Phys. Rev. B* **68**, 035405 (2003).
8. Hogan, C. et al. Optical properties of silicene, Si/Ag(111), and Si/Ag(110). *Phys. Rev. B* **97**, 195407 (2018).
9. Schmidt, W. G., Glutsch, S., Hahn, P. H. & Bechstedt, F. Efficient $\mathcal{O}(N^2)$ method to solve the Bethe-Salpeter equation. *Phys. Rev. B* **67**, 085307 (2003).
10. Landmann, M. et al. GaN *m*-plane: Atomic structure, surface bands, and optical response. *Phys. Rev. B* **91**, 035302 (2015).
11. Ruiz Alvarado, I. A., Zare Pour, M. A., Hannappel, T. & Schmidt, W. G. Structural fingerprints in the reflectance anisotropy of AlInP(001). *Phys. Rev. B* **108**, 045410 (2023).
12. Palummo, M., Witkowski, N., Pluchery, O., Del Sole, R. & Borensztein, Y. Reflectance-anisotropy spectroscopy and surface differential reflectance spectra at the Si(100) surface: Combined experimental and theoretical study. *Phys. Rev. B* **79**, 035327 (2009).
13. Hingerl, K., Balderas-Navarro, R. E., Bonanni, A., Tichopadek, P. & Schmidt, W. G. On the origin of resonance features in reflectance difference data of silicon. *Appl. Surf. Sci.* **175-176**, 769–776 (2001).
14. Sole, R. D. & Onida, G. Surface versus crystal-termination effects in the optical properties of surfaces. *Phys. Rev. B* **60**, 5523–5528 (1999).
15. Arciprete, F. et al. Surface versus bulk contributions from reflectance anisotropy and electron energy loss spectra of the GaAs(001) − *c*(4 × 4) surface. *Phys. Rev. B* **68**, 125328 (2003).
16. Hogan, C., Paget, D., Tereshchenko, O. E., Reining, L. & Onida, G. Optical anisotropy induced by cesium adsorption on the As-rich *c*(2 × 8) reconstruction of GaAs(001). *Phys. Rev. B* **69**, 125332 (2004).
17. Hingerl, K., Balderas-Navarro, R. E., Hilber, W., Bonanni, A. & Stifter, D. Surface-stress-induced optical bulk anisotropy. *Phys. Rev. B* **62**, 13048–13052 (2000).
18. Schmidt, W. G. et al. Understanding reflectance anisotropy: Surface-state signatures and bulk-related features in the optical spectrum of InP(001)(2 × 4). *Phys. Rev. B* **61**, R16335–R16338 (2000).
19. Schmidt, W. G., Bechstedt, F., Lu, W. & Bernholc, J. Interplay of surface reconstruction and surface electric fields in the optical anisotropy of GaAs(001). *Phys. Rev. B* **66**, 085334 (2002).
20. Acosta-Ortiz, S. E. & Lastras-Martínez, A. Electro-optic effects in the optical anisotropies of (001) GaAs. *Phys. Rev. B* **40**, 1426–1429 (1989).
21. Schmidt, W. et al. Calculation of surface optical properties: from qualitative understanding to quantitative predictions. *Thin Solid Films* **455–456**, 764–771 (2004).
22. Weightman, P., Martin, D. S., Cole, R. J. & Farrell, T. Reflection anisotropy spectroscopy. *Rep. Prog. Phys.* **68**, 1251–1341 (2005).
23. Aspnes, D. E., Mantese, L., Bell, K. A. & Rossow, U. Photon-induced localization and final-state correlation effects in optically absorbing materials. *J. Vac. Sci. Technol. B* **16**, 2367–2372 (1998).
24. Mantese, L., Xue, Q. K., Sakurai, T. & Aspnes, D. E. Analysis of high-index Si(001) surfaces by reflectance difference spectroscopy. *J. Vac. Sci. Technol. A* **17**, 1652–1656 (1999).

25. Mantese, L., Bell, K., Aspnes, D. & Rossow, U. Photon-induced localization in optically absorbing materials. *Phys. Lett. A* **253**, 93–97 (1999).
26. Rossow, U., Mantese, L. & Aspnes, D. E. Surface-induced optical anisotropy of Si and Ge. *J. Vac. Sci. Technol. B* **18**, 2229–2231 (2000).
27. Onida, G., Reining, L. & Rubio, A. Electronic excitations: density-functional versus many-body Green's-function approaches. *Rev. Mod. Phys.* **74**, 601–659 (2002).
28. Albrecht, S., Reining, L., Del Sole, R. & Onida, G. Ab initio calculation of excitonic effects in the optical spectra of semiconductors. *Phys. Rev. Lett.* **80**, 4510–4513 (1998).
29. Fuchs, F., Rödl, C., Schleife, A. & Bechstedt, F. Efficient $\mathcal{O}(N^2)$ approach to solve the Bethe-Salpeter equation for excitonic bound states. *Phys. Rev. B* **78**, 085103 (2008).
30. Gorelov, V. et al. Delocalization of dark and bright excitons in flat-band materials and the optical properties of $V_2O_5$. *Npj Comput. Mater.* **8**, 94 (2022).
31. Acharya, S. et al. A theory for colors of strongly correlated electronic systems. *Nat. Commun.* **14**, 5565 (2023).
32. Varrassi, L., Liu, P. & Franchini, C. Quasiparticle and excitonic properties of monolayer $SrTiO_3$. *Phys. Rev. Mater.* **8**, 024001 (2024).
33. Palummo, M. et al. The Bethe–Salpeter equation: a first-principles approach for calculating surface optical spectra. *J. Phys. Condens. Matter* **16**, S4313–S4322 (2004).
34. May, M. M. et al. The interface of GaP(100) and $H_2O$ studied by photoemission and reflection anisotropy spectroscopy. *New J. Phys.* **15**, 103003 (2013).
35. May, M. M., Lewerenz, H.-J. & Hannappel, T. Optical in situ study of InP(100) surface chemistry: Dissociative adsorption of water and oxygen. *J. Phys. Chem. C* **118**, 19032–19041 (2014).
36. May, M. M. & Sprik, M. Water adsorption on the P-rich GaP(100) surface: optical spectroscopy from first principles. *New J. Phys.* **20**, 033031 (2018).
37. Ostheimer, D. et al. Water vapor interaction with well-ordered GaInP(100) surfaces. *J. Phys. Chem. C* **128**, 19559–19569 (2024).
38. Supplie, O. et al. In situ characterization of interfaces relevant for efficient photoinduced reactions. *Adv. Mater. Interfaces* **4,**1601118 (2017).
39. Supplie, O. et al. Metalorganic vapor phase epitaxy of III-V-on-silicon: Experiment and theory. *Prog. Cryst. Growth Charact. Mater.* **64**, 103–132 (2018).
40. Paszuk, A. et al. GaAsP/Si tandem solar cells: In situ study on GaP/Si:As virtual substrate preparation. *Sol. Energy Mater. Sol. Cells* **180**, 343–349 (2018).
41. Paszuk, A. et al. Double-layer stepped Si(100) surfaces prepared in As-rich CVD ambience. *Appl. Surf. Sci.* **462**, 1002–1007 (2018).
42. Nandy, M. et al. A route to obtaining low-defect III-V epilayers on Si(100) utilizing MOCVD. *Cryst. Growth Des.* **21**, 5603–5613 (2021).
43. May, M. M. et al. On the benchmarking of multi-junction photoelectrochemical fuel generating devices. *Sustain. Energy Fuels* **1**, 492–503 (2017).
44. Alqahtani, M. et al. Heteroepitaxy of GaP on silicon for efficient and cost-effective photoelectrochemical water splitting. *J. Mater. Chem. A* **7**, 8550–8558 (2019).
45. Feifel, M. et al. Epitaxial GaInP/GaAs/Si triple–junction solar cell with 25.9% AM1.5g efficiency enabled by transparent metamorphic $Al_xGa_{1-x}As_yP_{1-y}$ step-graded buffer structures. *Sol. RRL* **5**, 2000763 (2021).
46. Hannappel, T. et al. Integration of multijunction absorbers and catalysts for efficient solar-driven artificial leaf structures: A physical and materials science perspective. *Sol. RRL* **8**, 2301047 (2024).
47. Uhrberg, R. I. G., Bringans, R. D., Bachrach, R. Z. & Northrup, J. E. Symmetric arsenic dimers on the Si(100) surface. *Phys. Rev. Lett.* **56**, 520–523 (1986).
48. Bohlemann, C. Y. et al. Surface structure of MOVPE-prepared As-modified Si(100) substrates. *Appl. Surf. Sci.* **675**, 160879 (2024).
49. Schmidt, W. G. Calculation of reflectance anisotropy for semiconductor surface exploration. *Phys. Stat. Solid. B* **242**, 2751–2764 (2005).
50. del Sole, R. Microscopic theory of optical properties of crystal surfaces. *Solid State Commun.* **37**, 537–540 (1981).
51. Del Sole, R. & Fiorino, E. Macroscopic dielectric tensor at crystal surfaces. *Phys. Rev. B* **29**, 4631–4645 (1984).
52. Manghi, F., Del Sole, R., Selloni, A. & Molinari, E. Anisotropy of surface optical properties from first-principles calculations. *Phys. Rev. B* **41**, 9935–9946 (1990).
53. Selci, S., Ciccacci, F., Chiarotti, G., Chiaradia, P. & Cricenti, A. Surface differential reflectivity spectroscopy of semiconductor surfaces. *J. Vac. Sci. Technol. A* **5**, 327–332 (1987).
54. Hingerl, K., Aspnes, D. E., Kamiya, I. & Florez, L. T. Relationship among reflectance-difference spectroscopy, surface photoabsorption, and spectroellipsometry. *Appl. Phys. Lett* **63**, 885–887 (1993).
55. Esser, N. et al. Atomic structure and optical anisotropy of III–V(001) surfaces. *J. Vac. Sci. Technol. B* **19**, 1756–1761 (2001).
56. Aspnes, D. E. & Studna, A. A. Dielectric functions and optical parameters of Si, Ge, GaP, GaAs, GaSb, InP, InAs, and InSb from 1.5 to 6.0 eV. *Phys. Rev. B* **27**, 985–1009 (1983).
57. Bechstedt, F. *Many-body approach to electronic excitations: Concepts and applications* (Springer, 2014).
58. Kresse, G. & Furthmüller, J. Efficient iterative schemes for ab initio total-energy calculations using a plane-wave basis set. *Phys. Rev. B* **54**, 11169–11186 (1996).
59. Kresse, G. & Joubert, D. From ultrasoft pseudopotentials to the projector augmented-wave method. *Phys. Rev. B* **59**, 1758–1775 (1999).
60. Blöchl, P. E. Projector augmented-wave method. *Phys. Rev. B* **50**, 17953–17979 (1994).
61. Heyd, J., Scuseria, G. E. & Ernzerhof, M. Hybrid functionals based on a screened Coulomb potential. *J. Chem. Phys.* **118**, 8207–8215 (2003).
62. Heyd, J., Scuseria, G. E. & Ernzerhof, M. Erratum: "Hybrid functionals based on a screened Coulomb potential" [J. Chem. Phys. 118, 8207 (2003)]. *J. Chem. Phys.* **124**, 219906 (2006).
63. Sagredo, F. et al. The reliability of hybrid functionals for accurate fundamental and optical gap prediction of bulk solids and surfaces. *J. Chem. Theory Comput.* **21**, 5009–5015 (2025).
64. Noffsinger, J., Kioupakis, E., Van de Walle, C. G., Louie, S. G. & Cohen, M. L. Phonon-assisted optical absorption in silicon from first principles. *Phys. Rev. Lett.* **108**, 167402 (2012).
65. Marini, A. Ab initio finite-temperature excitons. *Phys. Rev. Lett.* **101**, 106405 (2008).
66. Albrecht, S., Reining, L., Onida, G., Olevano, V. & Del Sole, R. Ab initio calculation of excitonic effects in the optical spectra of semiconductors. *Phys. Rev. Lett.* **83**, 3971–3971 (1999).
67. Palummo, M., Onida, G., Del Sole, R. & Mendoza, B. S. Ab initio optical properties of Si(100). *Phys. Rev. B* **60**, 2522–2527 (1999).
68. Hahn, P. H., Schmidt, W. G., Bechstedt, F., Pulci, O. & Del Sole, R. P-rich GaP(001)(2 × 1)/(2 × 2) surface: A hydrogen-adsorbate structure determined from first-principles calculations. *Phys. Rev. B* **68**, 033311 (2003).
69. Schmidt, W. G., Briggs, E. L., Bernholc, J. & Bechstedt, F. Structural fingerprints in the reflectance anisotropy spectra of InP(001)(2 × 4) surfaces. *Phys. Rev. B* **59**, 2234–2239 (1999).
70. Kumar, P. & Patterson, C. H. Dielectric anisotropy of the GaP/Si(001) interface from first-principles theory. *Phys. Rev. Lett.* **118**, 237403 (2017).
71. Perdew, J. P. et al. Restoring the density-gradient expansion for exchange in solids and surfaces. *Phys. Rev. Lett.* **100**, 136406 (2008).

72. Perdew, J. P. et al. Erratum: Restoring the density-gradient expansion for exchange in solids and surfaces [Phys. Rev. Lett. 100, 136406 (2008)]. *Phys. Rev. Lett.* **102**, 039902 (2009).
73. Fiorentini, V. & Methfessel, M. Extracting convergent surface energies from slab calculations. *J. Phys. Condens. Matter* **8**, 6525–6529 (1996).
74. Gajdoš, M., Hummer, K., Kresse, G., Furthmüller, J. & Bechstedt, F. Linear optical properties in the projector-augmented wave methodology. *Phys. Rev. B* **73**, 045112 (2006).
75. Sander, T., Maggio, E. & Kresse, G. Beyond the Tamm-Dancoff approximation for extended systems using exact diagonalization. *Phys. Rev. B* **92**, 045209 (2015).
76. Furthmüller, J., Bechstedt, F., Botti, S. & Cappellini, G. Influence of spin-orbit interaction and self-consistency on quasiparticle electronic structure and exciton optical spectra beyond Tamm-Dancoff: The case of $BaF_2$ and $SrF_2$. *Phys. Rev. B* **112**, 195112 (2025).
77. Bechstedt, F., Del Sole, R., Cappellini, G. & Reining, L. An efficient method for calculating quasiparticle energies in semiconductors. *Solid State Commun.* **84**, 765–770 (1992).
78. Hannappel, T., Visbeck, S., Töben, L. & Willig, F. Apparatus for investigating metalorganic chemical vapor deposition-grown semiconductors with ultrahigh-vacuum based techniques. *Rev. Sci. Instrum.* **75**, 1297–1304 (2004).
79. Lautenschlager, P., Garriga, M., Vina, L. & Cardona, M. Temperature dependence of the dielectric function and interband critical points in silicon. *Phys. Rev. B* **36**, 4821–4830 (1987).


## Acknowledgements

We thank the staff of the Compute Center of the Technische Universität Ilmenau, especially Mr. Henning Schwanbeck for providing an excellent research environment. M.G. would like to thank M. Grunert for asking thought-provoking questions, providing constructive feedback as a proof-reader, and contributing to a delightful and productive office atmosphere. This work is supported by the Carl-Zeiss-Stiftung (CZS, proj. *SustEn-Mat*, proj. no. P2023-02-008), the German Federal Ministry of Education and Research (BMBF, proj. *$H_2$Demo*, proj. no. 03SF0619I), and the DFG (TRR 142/3-2025, proj. no. 231447078). We acknowledge the Paderborn Center for Parallel Computing ($PC^2$) for grants of high-performance computer time.

## Author contributions

M.G. conceived the idea, carried out the calculations, analyzed the data, visualized all results, and wrote the first draft of the manuscript. E.R. suggested the model calculations. K.D.H. prepared the samples, performed the LEED, XPS, and LT RAS measurements and evaluated the experimental results. C.Y.B. assisted the sample preparation and evaluation of experimental results. A.P. advised the experimental planning. M.G., W.G.S., and E.R. discussed and interpreted the theoretical results. T.H., W.G.S., and E.R. supervised the work; all authors revised and approved the manuscript.

## Funding

Open Access funding enabled and organized by Projekt DEAL.

## Competing interests

The authors declare no competing interests.

## Additional information

**Supplementary information** The online version contains supplementary material available at https://doi.org/10.1038/s43246-026-01110-3.

**Correspondence** and requests for materials should be addressed to Max Großmann.

**Peer review information** *Communications Materials* thanks Bo Peng and the other, anonymous, reviewer(s) for their contribution to the peer review of this work. A peer review file is available.